

# PROCEEDINGS OF SPIE

[SPIDigitalLibrary.org/conference-proceedings-of-spie](https://spiedigitallibrary.org/conference-proceedings-of-spie)

## A fast Stokes polarimeter: preliminary design

Israel J. Vaughn, Andrey S. Alenin, J. Scott Tyo

**SPIE.**

# A fast Stokes polarimeter: preliminary design

Israel J. Vaughn<sup>a</sup>, Andrey S. Alenin<sup>a</sup>, J. Scott Tyo<sup>a</sup>

<sup>a</sup>University of New South Wales Canberra, ACT, Australia

## ABSTRACT

Designing polarimetric systems directly in the channel space has provided insight into how to design new types of polarimetric systems, including systems which use carriers in hybrid domains of space, time, or spectrum. Utilizing linear systems theory, we present a full Stokes imaging polarimeter design which has the potential to operate at half the frame rate of the imaging sensor of the system by utilizing a hybrid spatio-temporal carrier design. The design places channels on the faces and the edges of the Nyquist cube resulting in the potential for half the Nyquist limit to be achieved, provided that the spatial frequency of the objects being imaged are bandlimited to less than 0.25 cycles per pixel. If the objects are not spatially bandlimited, then the achievable temporal bandwidth is more difficult to analyze. However, a spatio-temporal tradeoff still exists allowing for increased temporal bandwidth. We present the design of a “Fast Stokes” polarimeter and some simulated images using this design.

**Keywords:** polarimetry, modulated polarimetry, linear systems, microanalyzer array, micropolarizer array, polarimetric channels

## 1. INTRODUCTION

Passive polarimetric instruments have been in use for quite some time, including for remote sensing tasks. Passive instruments are also called Stokes polarimeters, and both “full Stokes” and partial Stokes instruments have been built and deployed. Full Stokes imaging polarimeters measure the complete set of Stokes parameters across a scene. In optical wavelength measuring instruments, there are two general classes of strategies that can be employed. The first is to divide the light into separate optical paths that are analyzed by independent sets of polarization optics. The second strategy is to multiplex the information over the entire image in some way.<sup>1-3</sup> The general irradiance for a Stokes polarimeter can be described by the following equation:

$$s_{0,\text{out}}(\mathbf{x}) = a_0(\mathbf{x}) \cdot s_{0,\text{obj}}(\mathbf{x}) + a_1(\mathbf{x}) \cdot s_{1,\text{obj}}(\mathbf{x}) + a_2(\mathbf{x}) \cdot s_{2,\text{obj}}(\mathbf{x}) + a_3(\mathbf{x}) \cdot s_{3,\text{obj}}(\mathbf{x}). \quad (1)$$

The parameter set  $\mathbf{x}$  represents a set of independent variables such as space,<sup>3-6</sup> time,<sup>1,7,8</sup> wavelength,<sup>9</sup> angle of incidence,<sup>10</sup> etc., and the functions  $a_0(\mathbf{x}) - a_3(\mathbf{x})$  generate the carriers. Real instruments take discrete measurements, so the left hand side (LHS) of Equation (1) becomes a discrete point measurement, and these measurements can be concatenated into a  $n \times 1$  vector,  $\mathbf{g}_{s_{0,\text{out}}}$ , for  $n$  measurements of  $s_{0,\text{out}}(\mathbf{x}_j)$ . If  $\mathbf{A}(\mathbf{x})$  is known, then the right hand side (RHS) of Equation (1) can be rewritten as

$$\begin{bmatrix} a_{00}(\mathbf{x}_j) & a_{01}(\mathbf{x}_j) & a_{02}(\mathbf{x}_j) & a_{03}(\mathbf{x}_j) \end{bmatrix} \cdot \begin{bmatrix} s_{0,\text{obj}}(\mathbf{x}_j) \\ s_{1,\text{obj}}(\mathbf{x}_j) \\ s_{2,\text{obj}}(\mathbf{x}_j) \\ s_{3,\text{obj}}(\mathbf{x}_j) \end{bmatrix} \quad (2)$$

for each  $\mathbf{x}_j$ . Note  $\mathbf{a} = [a_{00}(\mathbf{x}_j) \ a_{01}(\mathbf{x}_j) \ a_{02}(\mathbf{x}_j) \ a_{03}(\mathbf{x}_j)]$  is the first row of the Mueller matrix of the polarizing optics in the polarization state analyzer (PSA), and is often denoted the “analyzer vector” due to the formal

---

Send correspondence to IJV  
IJV: israel.vaughn@gmail.com

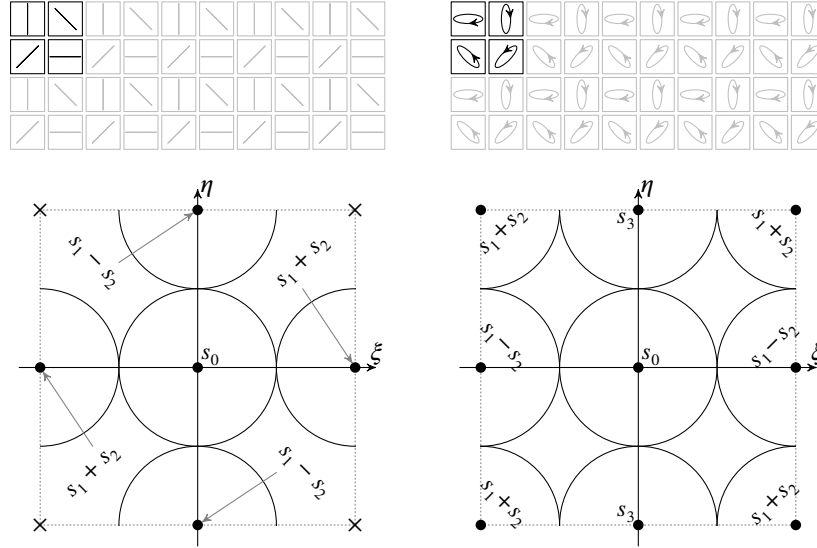


Figure 1: Fourier domain channels; (left) Conventional linearly polarized micropolarizer array. (right)  $2 \times 2$  full-Stokes microanalyzer design by Myhre *et al.*<sup>12</sup> Figure adapted from Alenin *et al.*<sup>5</sup>

projection of the measured Stokes parameters onto it. The term “analyze” refers to the projection operation itself. A system of equations can then be built up as:

$$\mathbf{g}_{s_{0,\text{out}}} = \begin{bmatrix} a_0(\mathbf{x}_0) & a_1(\mathbf{x}_0) & a_2(\mathbf{x}_0) & a_3(\mathbf{x}_0) \\ a_0(\mathbf{x}_1) & a_1(\mathbf{x}_1) & a_2(\mathbf{x}_1) & a_3(\mathbf{x}_1) \\ \vdots & \vdots & \vdots & \vdots \\ a_{00}(\mathbf{x}_{n-1}) & a_{01}(\mathbf{x}_{n-1}) & a_{02}(\mathbf{x}_{n-1}) & a_{03}(\mathbf{x}_{n-1}) \end{bmatrix} \cdot \begin{bmatrix} s_{0,\text{obj}}(\mathbf{x}_{\lfloor (n-1)/2 \rfloor}) \\ s_{1,\text{obj}}(\mathbf{x}_{\lfloor (n-1)/2 \rfloor}) \\ s_{2,\text{obj}}(\mathbf{x}_{\lfloor (n-1)/2 \rfloor}) \\ s_{3,\text{obj}}(\mathbf{x}_{\lfloor (n-1)/2 \rfloor}) \end{bmatrix} = \mathbf{W} \cdot \mathbf{s} \quad (3)$$

These equations require that a strong assumption holds;  $\mathbf{s}_{\text{obj}}(\mathbf{x})$  is approximately constant over the range  $\mathbf{x}_0, \mathbf{x}_1, \dots, \mathbf{x}_{n-1}$ .  $\lfloor \cdot \rfloor$  denotes the nearest integer function and  $\mathbf{A}$  is an  $n \times 4$  matrix.  $\mathbf{s}_{\text{obj}}(\mathbf{x})$  being constant is equivalent to  $\mathbf{s}_{\text{obj}}(\mathbf{x})$  having *zero bandwidth* extent in the channel domain.<sup>11</sup>

An equivalent expression for Eq. (1) is in the Fourier, or channel domain:

$$S_{0,\text{out}}(\boldsymbol{\rho}) = \sum_{j=0}^3 A_j(\boldsymbol{\rho}) * S_j(\boldsymbol{\rho}) \quad (4)$$

where  $*$  denotes convolution,  $\mathbf{x} \rightarrow \boldsymbol{\rho}$  are the Fourier dual variables,  $A_j$  are the Fourier transforms of the analyzer functions, and  $S_j$  are the Fourier transforms of the Stokes object functions. In this communication we use the spatio-temporal domain  $(x, y, t) \rightarrow (\xi, \eta, \nu)$ . When the functions  $a_{mn}$  are periodic in  $\mathbf{x}$ , then their Fourier transforms  $A_{mn}$  create a grid of  $\delta$ -functions in  $\boldsymbol{\rho}$ . We denote the resultant  $\delta$ -functions the system’s *channels*.

There is little analysis of spatio-temporal bandwidth of polarimetric instruments outside of our group,<sup>3-5,7,8,11</sup> with some recent focus by our group and others being on spatial or temporal bandwidth individually.<sup>2,3</sup> This communication presents a novel spatio-temporal analysis and an instrument design which uses a 3-channel linear division of focal plane (DoFP) polarimeter in combination with rotating retarders to allow spatial and temporal bandwidth to be traded off. The new system can create full Stokes images every two frames instead of every four for a standard division of time (DoT) system.

## 2. SPATIO-TEMPORAL DESCRIPTION

DoFP devices use unit cells of micropolarizing elements tiled over a focal plane array (FPA). While several recent studies have shown the value of using more complicated unit cells,<sup>2,3,5</sup> most systems being manufactured have

used  $2 \times 2$  unit cells. The most common layout is the arrangement of four linearly polarized states shown in Fig. 1 (left), though full-Stokes systems have also been made as shown in Fig. 2 (right).<sup>12</sup> More recently, the  $4 \times 2$  unit cell proposed by LeMaster and Hirakawa<sup>2</sup> has been shown to have improved bandwidth for linear polarimeters. These systems are “snapshot” polarimeters, in that they can estimate the Stokes parameters at every frame of the image sequence. This is accomplished giving up some spatial bandwidth.<sup>3</sup>

In an earlier study, LaCasse, *et al*, considered a full-Stokes system made up of a linear micropolarizer array, with a rotating retarder.<sup>13</sup> That system suffered from a severe temporal bandwidth penalty, since they used independent spatial and temporal demodulation. Here we describe systems that uses the linear micropolarizer array layouts shown in Fig. 1 (left) combined with rotating retarders but couples them with 2 rotating linear

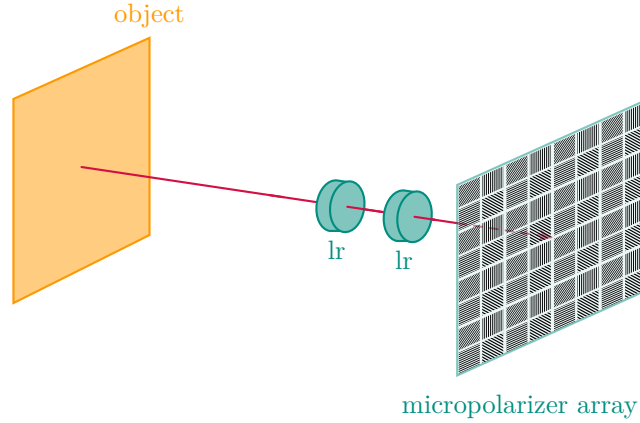


Figure 2: Schematic of the dual retarder + conventional micropolarizer array design. *lr* denotes a linear retarder. Note that the imaging optics are not shown here.

retarders (Fig. 1). These systems then use a spatio-temporal demodulation scheme that allows spatial and temporal resolution to be traded off.

We proceed to present the mathematical system description. However the algebraic details are tedious, so they are omitted here, but are shown in greater detail elsewhere.<sup>11</sup> We begin with the Stokes analyzer description of the micropolarizer array in Fig. 1A:

$$\mathbf{a} = \frac{1}{2} \begin{bmatrix} 1 & \frac{\cos \pi x + \cos \pi y}{2} & \frac{\cos \pi x - \cos \pi y}{2} & 0 \end{bmatrix}, \quad (5)$$

prior to sampling. Two rotating linear retarders can be represented by the Mueller matrix,  $\mathbf{RR}(v_k, v_l, \epsilon_k, \epsilon_l; \delta_k, \delta_l)$ <sup>11</sup>

$$\mathbf{RR}_{00} = 1, \quad \mathbf{RR}_{01} = \mathbf{RR}_{02} = \mathbf{RR}_{03} = \mathbf{RR}_{10} = \mathbf{RR}_{20} = \mathbf{RR}_{30} = 0 \quad (6)$$

$$\begin{aligned} \mathbf{RR}_{11} = & \left[ \cos^2 \frac{\delta_l}{2} + \sin^2 \frac{\delta_l}{2} \cos 8\pi(v_l t + \epsilon_l) \right] \left[ \cos^2 \frac{\delta_k}{2} + \sin^2 \frac{\delta_k}{2} \cos 8\pi(v_k t + \epsilon_k) \right] \\ & + \sin^2 \frac{\delta_l}{2} \sin^2 \frac{\delta_k}{2} \sin 8\pi(v_l t + \epsilon_l) \sin 8\pi(v_k t + \epsilon_k) \\ & - \sin \delta_l \sin \delta_k \sin 4\pi(v_l t + \epsilon_l) \sin 4\pi(v_k t + \epsilon_k) \end{aligned} \quad (7)$$

$$\begin{aligned} \mathbf{RR}_{12} = & \left[ \cos^2 \frac{\delta_l}{2} + \sin^2 \frac{\delta_l}{2} \cos 8\pi(v_l t + \epsilon_l) \right] \sin^2 \frac{\delta_k}{2} \sin 8\pi(v_k t + \epsilon_k) \\ & + \sin^2 \frac{\delta_l}{2} \sin 8\pi(v_l t + \epsilon_l) \left[ \cos^2 \frac{\delta_k}{2} - \sin^2 \frac{\delta_k}{2} \cos 8\pi(v_k t + \epsilon_k) \right] \\ & + \sin \delta_l \sin \delta_k \sin 4\pi(v_l t + \epsilon_l) \cos 4\pi(v_k t + \epsilon_k) \end{aligned} \quad (8)$$

$$\begin{aligned}
RR_{13} = & - \left[ \cos^2 \frac{\delta_l}{2} + \sin^2 \frac{\delta_l}{2} \cos 8\pi(\nu_l t + \varepsilon_l) \right] \sin \delta_k \sin 4\pi(\nu_k t + \varepsilon_k) \\
& + \sin^2 \frac{\delta_l}{2} \sin \delta_k \sin 8\pi(\nu_l t + \varepsilon_l) \cos 4\pi(\nu_k t + \varepsilon_k) \\
& - \sin \delta_l \cos \delta_k \sin 4\pi(\nu_l t + \varepsilon_l)
\end{aligned} \tag{9}$$

$$\begin{aligned}
RR_{21} = & \sin^2 \frac{\delta_l}{2} \sin 8\pi(\nu_l t + \varepsilon_l) \left[ \cos^2 \frac{\delta_k}{2} + \sin^2 \frac{\delta_k}{2} \cos 8\pi(\nu_k t + \varepsilon_k) \right] \\
& + \left[ \cos^2 \frac{\delta_l}{2} - \sin^2 \frac{\delta_l}{2} \cos 8\pi(\nu_l t + \varepsilon_l) \right] \sin^2 \frac{\delta_k}{2} \sin 8\pi(\nu_k t + \varepsilon_k) \\
& + \sin \delta_l \sin \delta_k \cos 4\pi(\nu_l t + \varepsilon_l) \sin 4\pi(\nu_k t + \varepsilon_k)
\end{aligned} \tag{10}$$

$$\begin{aligned}
RR_{22} = & \sin^2 \frac{\delta_l}{2} \sin^2 \frac{\delta_k}{2} \sin 8\pi(\nu_l t + \varepsilon_l) \sin 8\pi(\nu_k t + \varepsilon_k) \\
& + \left[ \cos^2 \frac{\delta_l}{2} - \sin^2 \frac{\delta_l}{2} \cos 8\pi(\nu_l t + \varepsilon_l) \right] \left[ \cos^2 \frac{\delta_k}{2} - \sin^2 \frac{\delta_k}{2} \cos 8\pi(\nu_k t + \varepsilon_k) \right] \\
& - \sin \delta_l \sin \delta_k \cos 4\pi(\nu_l t + \varepsilon_l) \cos 4\pi(\nu_k t + \varepsilon_k)
\end{aligned} \tag{11}$$

$$\begin{aligned}
RR_{23} = & - \sin^2 \frac{\delta_l}{2} \sin \delta_k \sin 8\pi(\nu_l t + \varepsilon_l) \sin 4\pi(\nu_k t + \varepsilon_k) \\
& + \left[ \cos^2 \frac{\delta_l}{2} - \sin^2 \frac{\delta_l}{2} \cos 8\pi(\nu_l t + \varepsilon_l) \right] \sin \delta_k \cos 4\pi(\nu_k t + \varepsilon_k) \\
& + \sin \delta_l \cos \delta_k \cos 4\pi(\nu_l t + \varepsilon_l)
\end{aligned} \tag{12}$$

$$\begin{aligned}
RR_{31} = & \sin \delta_l \sin 4\pi(\nu_l t + \varepsilon_l) \left[ \cos^2 \frac{\delta_k}{2} + \sin^2 \frac{\delta_k}{2} \cos 8\pi(\nu_k t + \varepsilon_k) \right] \\
& - \sin \delta_l \sin^2 \frac{\delta_k}{2} \cos 4\pi(\nu_l t + \varepsilon_l) \sin 8\pi(\nu_k t + \varepsilon_k) \\
& + \cos \delta_l \sin \delta_k \sin 4\pi(\nu_k t + \varepsilon_k)
\end{aligned} \tag{13}$$

$$\begin{aligned}
RR_{32} = & \sin \delta_l \sin^2 \frac{\delta_k}{2} \sin 4\pi(\nu_l t + \varepsilon_l) \sin 8\pi(\nu_k t + \varepsilon_k) \\
& - \sin \delta_l \cos 4\pi(\nu_l t + \varepsilon_l) \left[ \cos^2 \frac{\delta_k}{2} - \sin^2 \frac{\delta_k}{2} \cos 8\pi(\nu_k t + \varepsilon_k) \right] \\
& - \cos \delta_l \sin \delta_k \cos 4\pi(\nu_k t + \varepsilon_k)
\end{aligned} \tag{14}$$

$$\begin{aligned}
RR_{33} = & - \sin \delta_l \sin \delta_k \sin 4\pi(\nu_l t + \varepsilon_l) \sin 4\pi(\nu_k t + \varepsilon_k) \\
& - \sin \delta_l \sin \delta_k \cos 4\pi(\nu_l t + \varepsilon_l) \cos 4\pi(\nu_k t + \varepsilon_k) \\
& + \cos \delta_l \cos \delta_k
\end{aligned} \tag{15}$$

where  $RR_{kl}$  are elements of  $\mathbf{RR}$ ;  $\nu_k, \nu_l$  are the rotation rates of the first and second retarders respectively;  $\varepsilon_k, \varepsilon_l$  are the initial angular offsets from the laboratory frame of the first and second retarder respectively; and  $\delta_k, \delta_l$  are the retardances of the first and second retarders respectively. Combining the dual retarder with the conventional

Table 1: Channel notation.

	positive	negative
real		
imaginary		

micropolarizer array, Fig. 1A results in the analyzer vector

$$\frac{1}{2} \begin{bmatrix} 1 \\ a_1 \\ a_2 \\ a_3 \end{bmatrix} = \frac{1}{4} \begin{bmatrix} 2 \\ \cos \pi x (RR_{11} + RR_{21}) + \cos \pi y (RR_{11} - RR_{21}) \\ \cos \pi x (RR_{12} + RR_{22}) + \cos \pi y (RR_{12} - RR_{22}) \\ \cos \pi x (RR_{13} + RR_{23}) + \cos \pi y (RR_{13} - RR_{23}) \end{bmatrix} \quad (16)$$

generally. We know that  $\mathbf{X}^T \mathbf{p}$  for some arbitrary Mueller matrix element  $\mathbf{X}$  results in the final analyzer vector,<sup>11</sup> allowing us to solve the equation

$$\mathbf{X}^T \mathbf{p} = \frac{1}{2} \begin{bmatrix} 1 \\ c_1 \cos 2\pi y \cos(\pi t) \\ c_2 \cos 2\pi y \sin(\pi t) \\ c_3 \cos \pi x \end{bmatrix}. \quad (17)$$

See Appendix A in Vaughn<sup>11</sup> for a detailed derivation of the dual retarder carrier generation and the associated channel descriptions. Setting  $\delta_k = \pi/2, \delta_l = \pi, v_k = v_0, v_\ell = v_0/2, \epsilon_k = 0, \epsilon_\ell = -0.03125$ , or  $\delta_k = \pi, \delta_l = \pi/2, v_k = v_0, v_\ell = 0, \epsilon_k = 0.03125, \epsilon_\ell = -0.0625$ , where  $v_0$  is the reference rotation rate, results in

$$RR_{11} + RR_{21} = 0, \quad RR_{11} - RR_{21} = \frac{\sqrt{2}}{2} \cos(4\pi v_0 t) \quad (18)$$

$$RR_{12} + RR_{22} = 0, \quad RR_{12} - RR_{22} = \frac{\sqrt{2}}{2} \sin(4\pi v_0 t) \quad (19)$$

$$RR_{13} + RR_{23} = -\sqrt{2}, \quad RR_{13} - RR_{23} = 0 \quad (20)$$

$$\frac{1}{2} \begin{bmatrix} 1 \\ a_1 \\ a_2 \\ a_3 \end{bmatrix} = \frac{1}{4} \begin{bmatrix} 2 \\ \frac{\sqrt{2}}{2} \cos \pi y \cos(4\pi v_0 t) \\ \frac{\sqrt{2}}{2} \cos \pi y \sin(4\pi v_0 t) \\ -\sqrt{2} \cos \pi x \end{bmatrix} \text{ or } \frac{1}{4} \begin{bmatrix} 2 \\ \frac{\sqrt{2}}{2} \cos \pi y \sin(4\pi v_0 t) \\ -\frac{\sqrt{2}}{2} \cos \pi y \cos(4\pi v_0 t) \\ \sqrt{2} \cos \pi y \end{bmatrix} \quad (21)$$

respectively. We denote this class of conventional micropolarizer array + dual rotating retarder CoRR systems. Taking the 3-dimensional Fourier transform of the analyzer vector with  $v_0$  set so that we are sampling at the temporal Nyquist rate results in 3-dimensional  $\delta$ -functions or channels with locations on the faces and edges of the Nyquist cube, see the left column of Fig. 3. The  $s_1, s_2$  channels are located at  $(0, \pm 1/2, \pm 1/2)$  and the  $s_3$  channels are located at  $(\pm 1/2, 0, 0)$ . This channel structure shows that, in the ideal case, if the Stokes parameters images are spatially bandlimited to less than 0.25 cycles per pixel (the same bandwidth limitation of the underlying micropolarizer array), then we have the full temporal bandwidth available for the object reconstruction for all of the Stokes parameters. The issue with this channel structure is that the quadrature (sine) component for  $s_2$  will be sampled as zeros when sampling at the temporal Nyquist rate.

The problem with the system shown on the left side of Fig. 3 is that the  $s_1$  and  $s_2$  sidebands appear in the corners of the  $\eta - \nu$  plane. Since the system is sampled, the periodic nature of the discrete Fourier transform makes it impossible to reconstruct both the in-phase and quadrature components at the Nyquist frequency.

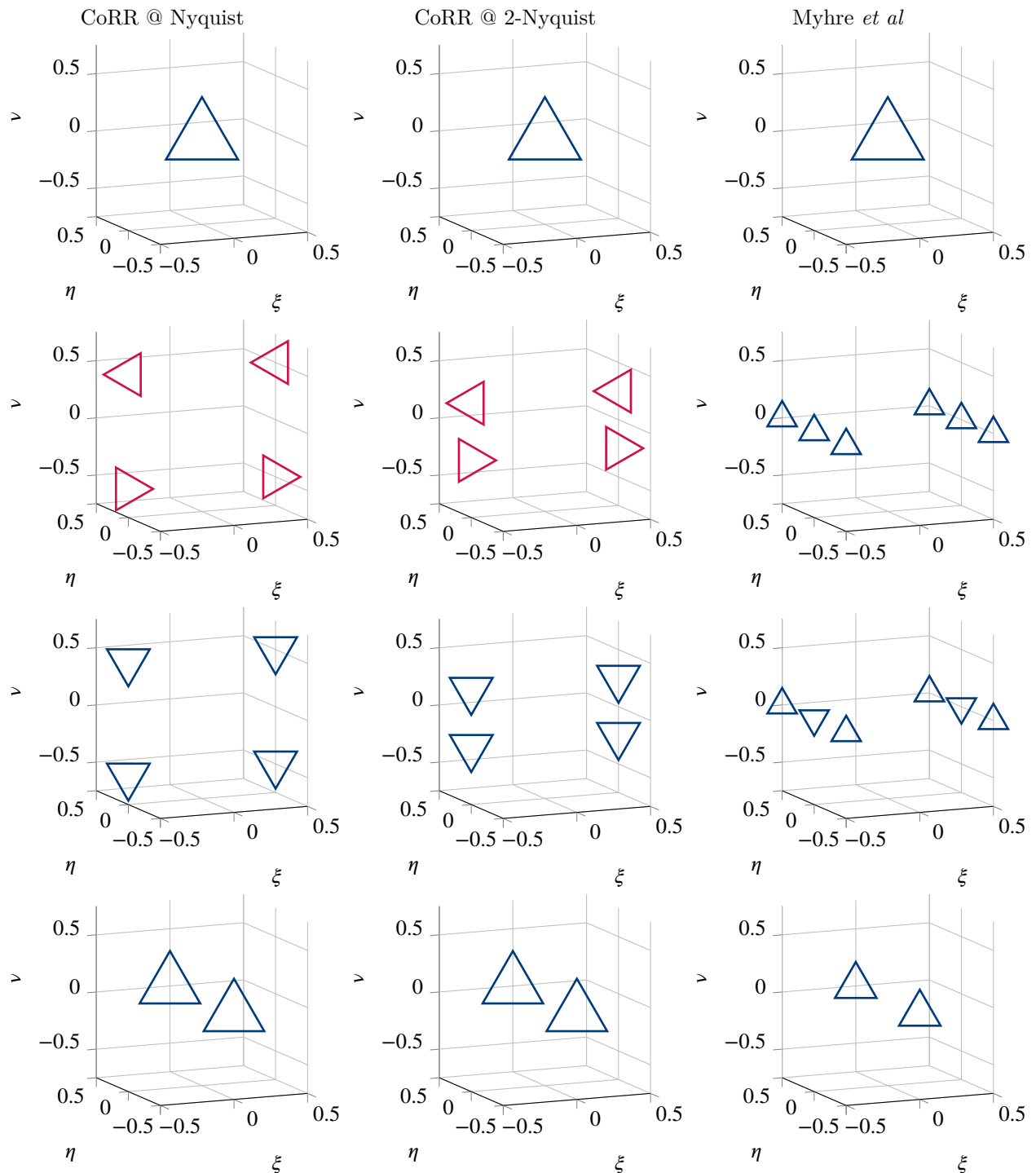


Figure 3: Channel structure for a dual retarder + micropolarizer array system. When sampled at Nyquist (left) the system is a partial Stokes due to the quadrature component. Sampling at twice Nyquist (center) results in a full Stokes system. For comparison the snapshot system from Myhre *et al*<sup>12</sup> is shown (right).

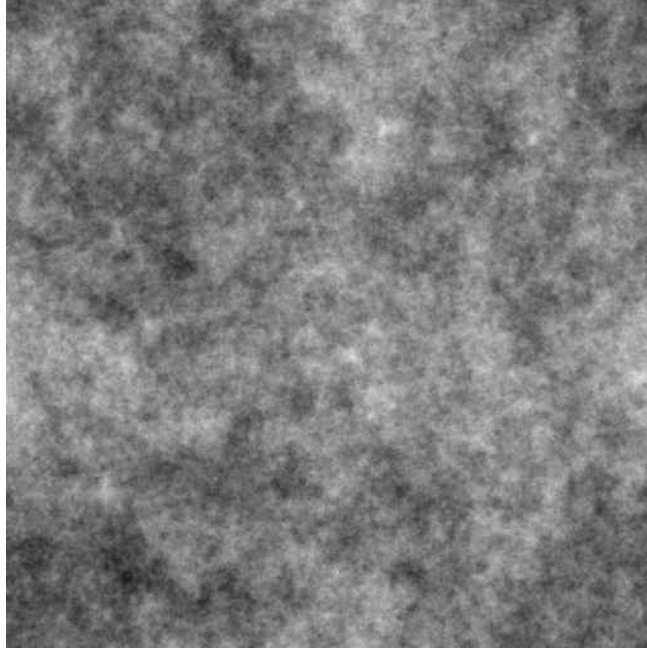


Figure 4: Sample of an truth Stokes parameters from a PSD with  $1/f^{3.073}$  statistics.

Doubling the sampling rate results in the channel structure shown in the right column of Fig. 3. By placing the side bands in on the faces Nyquist cube, we can now reconstruct both the in-phase and quadrature components. The full spatio-temporal bandwidth can be determined by looking at the distance between channel centers in 3-D space, but it is also reasonable to consider the projection of the sidebands into the spatial frequency plane. In this case, the system is able to produce full Stokes images at the half of the full temporal resolution of the imager, and this is accomplished by reducing the spatial bandwidth by 50%.

It is worth a brief discussion of how this system is able to create full Stokes reconstructions from partial Stokes MPAs. The second retarder (closest to the MPA) is a half-wave plate rotating at rate  $\nu_0/2$ . This has the effect of rotating the effective direction of the polarizers in the MPA at rate  $\nu_0$ . The other retarder is a quarter-waveplate (QWP) that is also rotating at rate  $\nu_0$ . The QWP is clocked so that it converts two of the orientations in the MPA into circular polarizers, and does nothing to the other two orientations.

### 3. SIMULATED DATA

We use a forward model which only relies on the well defined Mueller calculus<sup>14</sup> with two rotating retarders and the Mueller matrices of linear polarizers at each pixel. We use the retarder parameters defined in Section 2 and an ideal micropolarizer array of size  $512 \times 512$  pixels.

Natural images have power spectral density distributions (PSD) which are proportional to  $\approx 0.94/f^{2.073}$  both spatially and temporally,<sup>15</sup> we generate random spatio-temporal realizations from a  $1/f^{3.073}$  distribution and use them in the analysis and simulation for this section, details are in Vaughn *et al.*,<sup>16</sup> including the reason for the change in exponent from 2.073 (spatial distributions) to 3.073 (spatio-temporal distributions). These samples assume natural scenes and natural motion (e.g. trees moving in the wind), but do not properly represent motion or spatial statistics of scenes such as cars moving in a city. Figure 4 shows a sample of the kind of image used for our simulations. Note that to date, no empirical study has been published which determines typical statistics for full Stokes images or Mueller matrix images. Due to this lack of empirical data, we make an educated guess that natural scene Stokes data will follow natural scene spectral data. The covariance matrix used to generate

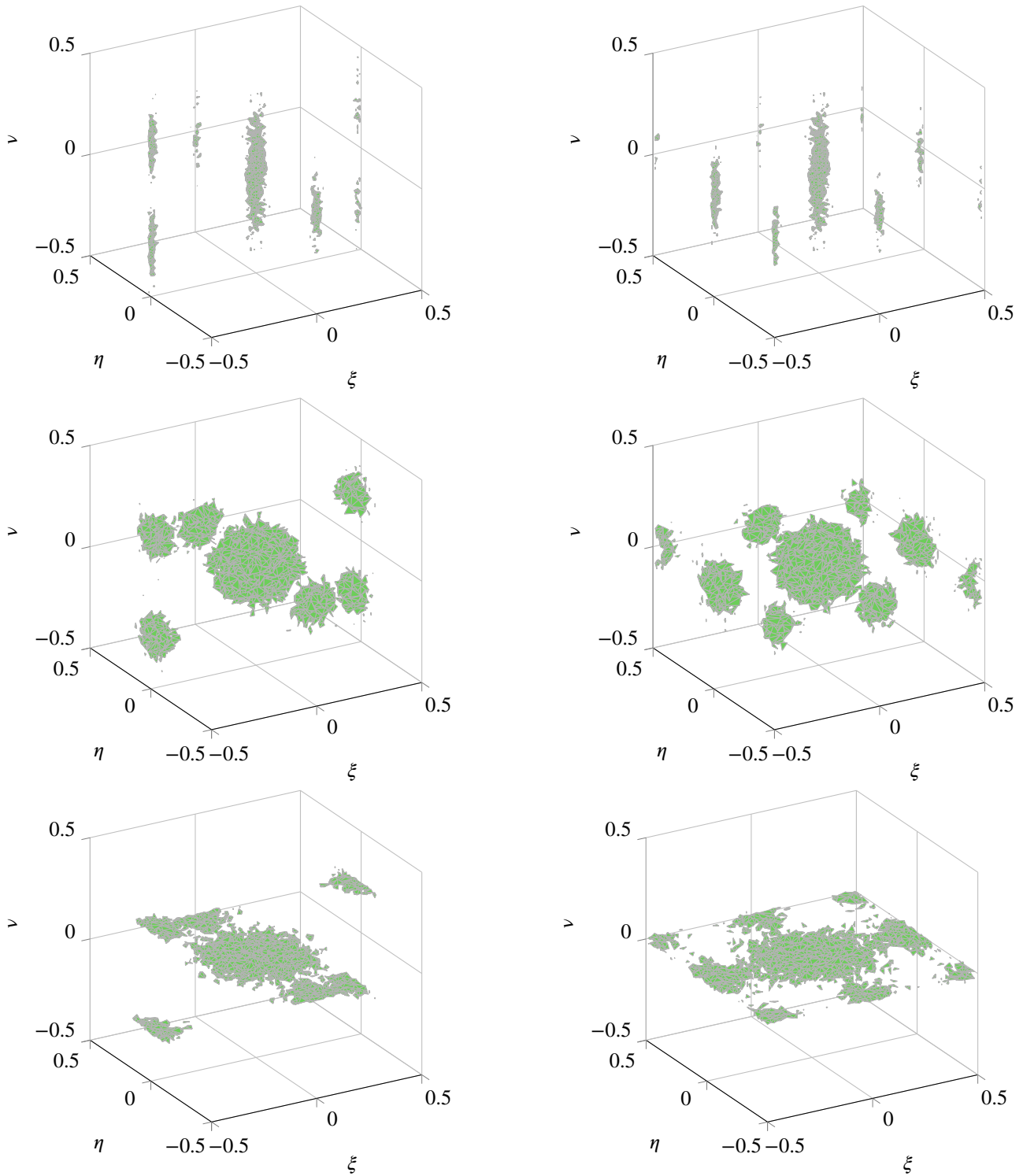


Figure 5: Magnitude of the Fourier transform of an instance of simulation data of (top row) the low spatial to temporal bandwidth case, (center row) the 1-to-1 spatial to temporal bandwidth case, and (bottom row) the high spatial to temporal bandwidth case. The left column shows the CoRR system, and the right column shows the Myhre *et al* (MHP) system. The isosurfaces are for the same constant value in all plots. Note that the data is placed at the channel locations.

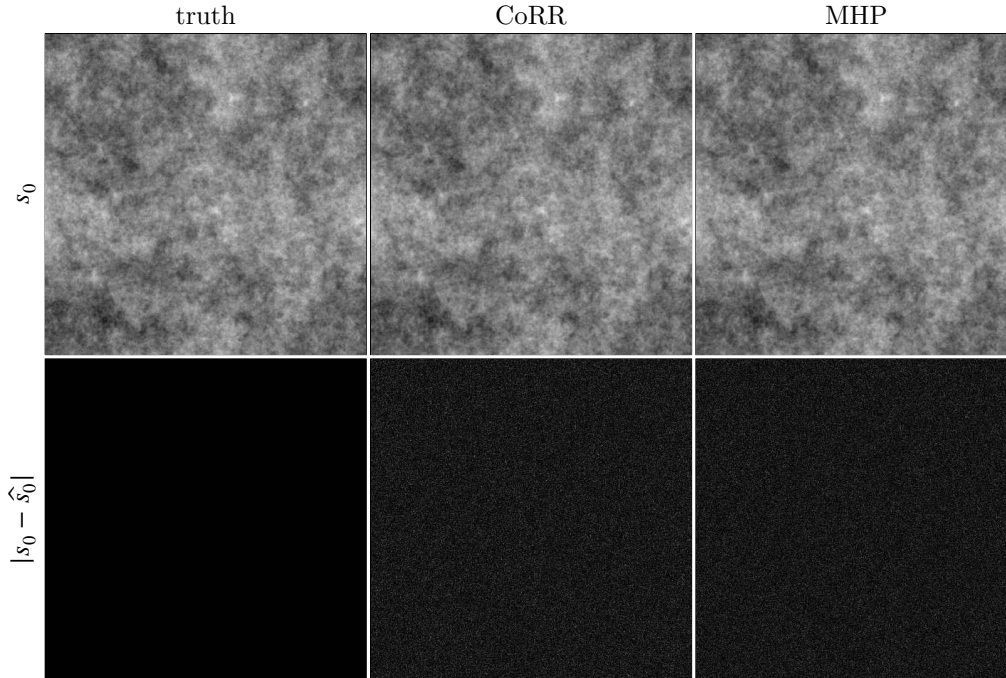


Figure 6: Reconstruction of  $s_0$  using optimized Fourier domain (FD) filters for the low spatial to temporal bandwidth case. The input data is shown on the top left, with the top row showing reconstructions and the bottom row showing the absolute difference between the truth and the input data. Our proposed conventional + rotating retarder (CoRR) design is shown in the center column, and the snapshot design by Myhre *et al*<sup>12</sup> is shown in the right column.

the data is:

$$\Sigma = \begin{bmatrix} 500 & 200 & 200 & 100 \\ 200 & 350 & -100 & 50 \\ 200 & -100 & 350 & 50 \\ 100 & 50 & 50 & 200 \end{bmatrix}. \quad (22)$$

This matrix quantifies the correlations between the Stokes parameters.

Image cubes with the spatio-temporal image statistics are generated and used as an object, passed through the forward imaging simulation, then Fourier transformed, filtered, unmixed, and finally inverse Fourier transformed to obtain the image estimate. Unmixing methods are detailed by our group in other literature<sup>3,5,7</sup> and won't be reviewed here. Relative bandwidths between space and time can be adjusted to simulate high spatial to temporal and low spatial to temporal bandwidth situations.

### 3.1 Simulated instrument reconstructions

In this section we compare the dual rotating retarder instrument with a full Stokes snapshot system proposed by Myrhe *et al*<sup>12</sup> shown in Fig. 1. A low spatial to temporal bandwidth example, a 1-to-1 spatial to temporal bandwidth example, and a high spatial to temporal bandwidth example are compared. Examples of the magnitude of the Fourier transformed data for different bandwidth scenarios are shown in Fig. 5 for 32 images of  $512 \times 512$  pixels. Notice that we expect the Myrhe *et al* system to perform well on the low spatial to temporal bandwidth data, and worse on the high spatial to temporal bandwidth data.

The system performance of the full Stokes systems was quantified as follows:

- Sets of 32 image blocks of size  $64 \times 64 \times 64$  were generated from the statistical generation algorithms.<sup>16</sup>

- A particle swarm algorithm was used to optimize linear Fourier domain (FD) filters for  $s_0$  and the sideband channels separately for each system and each bandwidth type, using the average PSNR<sup>17</sup> from the 32 image blocks as the cost function. The optimization used the cost function of PSNR for  $s_0$  and PSNR for the DoP for the sideband filters independently.
- The mean PSNR for each system was recorded for both systems for each bandwidth type. Over 200,000 cost function evaluations were computed.
- Final datasets of size  $512 \times 512 \times 64$ , ( $x \times y \times t$ ), were generated and reconstructed using the optimal FD filters for visualization purposes for the low spatial to temporal bandwidth case (Figs. 6 and 7). We can increase the pixel size because the statistical distribution is approximately scale invariant.

The low spatial to temporal bandwidth case should, intuitively, be better reconstructed by the Myhre *et al* (MHP) system, and this is shown qualitatively in Table 2a, particularly for the DoP PSNR. The DoP PSNR is about  $5.5dB$  better when using the MPH system as opposed to the CoRR system. The  $s_0$  PSNR values, are however, similar between the two systems. An example of the reconstructed output and the truth data is shown in Fig. 6 for the  $s_0$  data and in Fig. 7 for the DoP data. Notice the larger errors in the difference image in DoP of the CoRR system as compared with the MHP system. For the low spatial to temporal bandwidth case the MHP system achieves better performance.

For the 1-to-1 spatial to temporal bandwidth case it is unclear at first glance which system will perform better, although it appears that there should be less crosstalk between the  $s_1, s_2$  channels and the  $s_0$  channel for the CoRR system compared with the MHP system. The qualitative results are shown in Table 2b. The  $s_0$  PSNR is about  $0.5dB$  better when using the CoRR system as opposed to the MHP system. The DoP PSNR values, are however,  $1.4dB$  better for the MHP system. Overall, the system performance is similar between the MHP and CoRR systems for the 1-to-1 spatial to temporal bandwidth case.

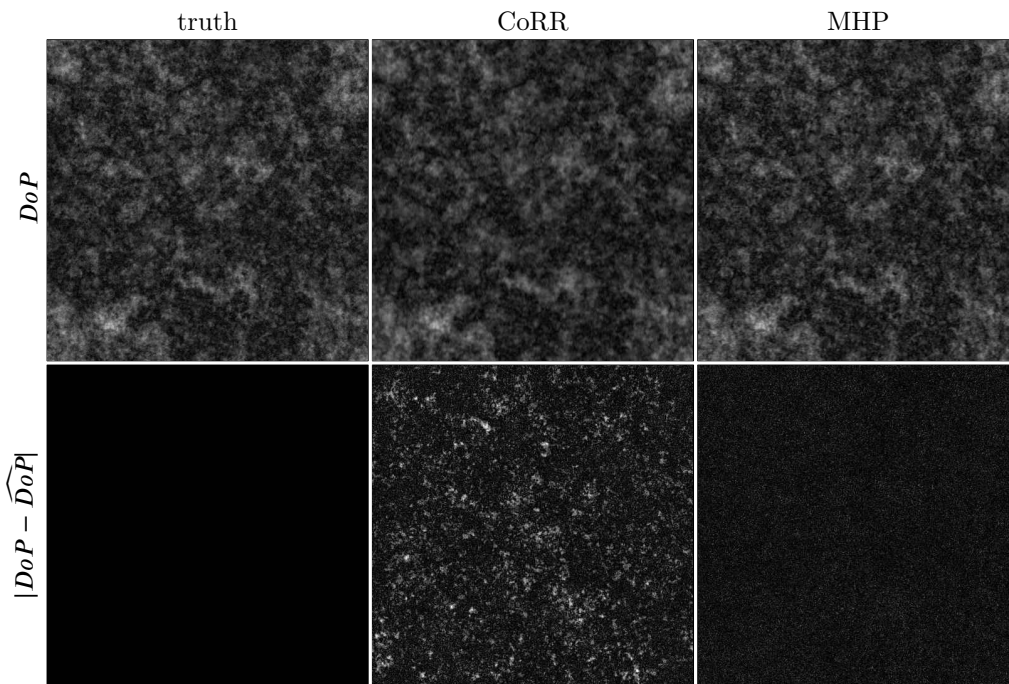


Figure 7: Reconstruction of the degree of polarization, DoP, using optimized Fourier domain (FD) filters for the low spatial to temporal bandwidth case. The input data is shown on the top left, with the top row showing reconstructions and the bottom row showing the absolute difference between the truth and the input data. Our proposed conventional + rotating retarder (CoRR) design is shown in the center column, and the snapshot design by Myhre *et al*<sup>12</sup> is shown in the right column.

Table 2:  $s_0$  and DoP PSNR results for the various bandwidth scenarios. The highest PSNR values are highlighted in yellow.

(a) low spatial to temporal bandwidth PSNR values ( $dB$ ).			(b) 1-to-1 spatial to temporal bandwidth PSNR values ( $dB$ ).			(c) high spatial to temporal bandwidth PSNR values ( $dB$ ).		
	CoRR	MHP		CoRR	MHP		CoRR	MHP
$s_0$	53.4	53.7	$s_0$	38.2	37.8	$s_0$	45.7	40.7
DoP	28.8	34.3	DoP	22.9	24.3	DoP	31.7	24.2

The channel structures suggest that for the high spatial to temporal bandwidth case the CoRR system will perform better than the MHP system. The qualitative results are shown in Table 2c. The DoP PSNR is about  $7.5dB$  better when using the CoRR system as opposed to the MPH system, and the  $s_0$  PSNR values are  $5db$  better. This shows that for a system which measures high spatial to temporal bandwidth, the CoRR system has potential to be much better than the snapshot MPH system.

#### 4. CONCLUSION

We have presented the analysis and design of a novel spatio-temporal full Stokes system which can be built using COTS micropolarizer arrays and rotating retarders (CoRR). Custom snapshot full Stokes instruments, like the one presented by Myhre *et al*<sup>12</sup> (MPH) can achieve better performance for low spatial to temporal bandwidth spatio-temporal data distributions, however our CoRR system is less expensive to build and can exceed the performance of the MHP system for the high spatial to temporal bandwidth case. For The 1-to-1 bandwidth case the two systems have similar performance results. The above results assume natural image scene statistics, it is unclear which system would perform better for city scenes, however we suspect that city and manmade landscapes would have a high spatial to temporal bandwidth in general, which would favor the CoRR system over the MPH snapshot system. Future work includes characterizing the prototype system which we are currently building, and analyzing the effects of systematic errors on the imaging scheme. We would also like to build a spatio-temporally channeled polarimeter which utilizes spatial channels in a way analogous to the double Nyquist temporal sampling, i.e., temporally Nyquist sampled with FPA spatial samples at twice the spatial Nyquist rate.

#### ACKNOWLEDGMENTS

This work was funded by the Asian Office of Aerospace Research and Development (FA2386-15-1-4098).

#### REFERENCES

- [1] LaCasse, C. F., Chipman, R. A., and Tyo, J. S., “Band limited data reconstruction in modulated polarimeters,” *Opt. Express* **19**, 14976–14989 (Aug 2011).
- [2] LeMaster, D. A. and Hirakawa, K., “Improved microgrid arrangement for integrated imaging polarimeters,” *Optics letters* **39**(7), 1811–1814 (2014).
- [3] Vaughn, I. J., Alenin, A. S., and Tyo, J. S., “Focal plane filter array engineering I: rectangular lattices,” *Optics Express* **25**(10), 11954–11968 (2017).
- [4] Vaughn, I. J., Alenin, A. S., and Tyo, J. S., “Bounds on the micropolarizer array channel assumption,” *SPIE Commercial + Scientific Sensing and Imaging*, 83640S–83640S, International Society for Optics and Photonics (2016).
- [5] Alenin, A. S., Vaughn, I. J., and Tyo, J. S., “Optimal bandwidth micropolarizer arrays,” *Optics Letters* **42**(3), 458–461 (2017).
- [6] Kudenov, M. W., Pezzaniti, L., Dereniak, E. L., and Gerhart, G. R., “Prismatic imaging polarimeter calibration for the infrared spectral region,” *Optics Express* **16**, 13720 – 13737 (2008).

- [7] Vaughn, I. J., Rodríguez-Herrera, O. G., Xu, M., and Tyo, J. S., “A portable imaging mueller matrix polarimeter based on a spatio-temporal modulation approach: theory and implementation,” *Proc. SPIE* **9613** (2015).
- [8] Vaughn, I. J., Rodríguez-Herrera, O. G., Xu, M., and Tyo, J. S., “Bandwidth and crosstalk considerations in a spatio-temporally modulated polarimeter,” *Proc. SPIE* **9613** (2015).
- [9] Oka, K. and Kato, T., “Spectroscopic polarimetry with a channeled spectrum,” *Optics Letters* **24**(21), 1475–1477 (1999).
- [10] Wakayama, T., Komaki, K., Vaughn, I. J., Tyo, J. S., Otani, Y., and Yoshizawa, T., “Evaluation of mueller matrix of achromatic axially symmetric wave plate,” *SPIE Optical Engineering+ Applications* , 88730P–88730P, International Society for Optics and Photonics (2013).
- [11] Vaughn, I., *Bandwidth and Noise in Spatio-temporally Modulated Mueller Matrix Polarimeters*, PhD thesis, College of Optical Sciences, University of Arizona (2016). Appendix A.
- [12] Myhre, G., Hsu, W.-L., Peinado, A., LaCasse, C., Brock, N., Chipman, R. A., and Pau, S., “Liquid crystal polymer full-stokes division of focal plane polarimeter,” *Opt. Express* **20**, 27393–27409 (Dec 2012).
- [13] LaCasse, C. F., Ririe, T., Chipman, R. A., and Tyo, J. S., “Spatio-temporal modulated polarimetry,” *Proc. SPIE* **8160**, 81600K–81600K–11 (2011).
- [14] Chipman, R., “Ch. 14 : Mueller matrices,” in [*Handbook of Optics Volume I: Geometrical and Physical Optics, Polarized Light, Components and Instruments*], Bass, M., ed., McGraw Hill, New York, third ed. (2009).
- [15] Torralba, A. and Oliva, A., “Statistics of natural image categories,” *Network: computation in neural systems* **14**(3), 391–412 (2003).
- [16] Vaughn, I. J., Alenin, A. S., and Tyo, J. S., “Statistical scene generation for polarimetric imaging systems,” *arXiv preprint arXiv:1707.02723* (2017).
- [17] Wang, Z. and Bovik, A. C., “Mean squared error: Love it or leave it? A new look at signal fidelity measures,” *IEEE Signal Process. Mag.* **26**, 98–117 (Jan 2009).